Journal of Solid State Chemistry 181 (2008) 2231–2236

Contents lists available at ScienceDirect

Journal of Solid State Chemistry

journal homepage: www.elsevier.com/locate/jssc

Synthesis of nanospherical Fe_3BO_6 anode material for lithium-ion battery by the rheological phase reaction method

Xixi Shi, Caixian Chang, Jiangfeng Xiang, Yong Xiao, Liangjie Yuan *, Jutang Sun

College of Chemistry and Molecular Sciences, Wuhan University, Wuhan 430072, P.R. China

ARTICLE INFO

Article history:
Received 29 February 2008
Received in revised form
6 May 2008
Accepted 11 May 2008
Available online 21 May 2008

Keywords:
Lithium-ion battery
Fe_3Bo_6
Nanospherical
Rheological phase reaction method
Anode material

ABSTRACT

This paper developed a novel method, the rheological phase reaction method, to synthesize nanospherical Fe_3BO_6. The sizes and morphologies of products vary with the calcination temperatures. Spherical particles with a uniform size about 40 nm in a monodisperse state were obtained at 800 °C, while the spherical particles with a larger size of 100–500 nm were obtained at 900 °C. The electrochemical properties of these Fe_3BO_6 nanospheres were investigated. Sample synthesized at 800 °C delivers a high reversible capacity above 500 mAh g^{-1}. Sample synthesized at 900 °C possesses relatively good cycleability with a capacity retaining of 376 mAh g^{-1} after 10 cycles. The measurement of electrochemical impedance spectra for the first time indicated that smaller Fe_3BO_6 nanoparticles intend to give higher impedance of solid-electrolyte interface layer and lower charge-transfer impedance after the first discharge. Additionally, it can be speculated that the increase of resistance charge-transfer is the possible reason for the capacity fading during cycling.

1. Introduction

Many efforts have been devoted to the research on lithium-ion battery for its wide applications in high-end consumer electronic products, and also for its promising use as the power source for electric and hybrid vehicles [1,2]. Much research work is presently directed towards the exploration of different types of materials to meet the ongoing market innovations. The iron-based materials, such as $LiFePO_4$ [3,4], Fe_2O_3 [5,6], Fe_3O_4 [7,8], $LiFeO_2$ [9], Li_2FeSiO_4 [10], etc., have been studied because of their low cost and environment-friendly character of iron. $LiFePO_4$ has been shown as the most prominent cathode material for lithium-ion battery.

In 2001, Nazar et al. [11] gave the first electrochemical investigation of Fe_3BO_6, which is cheap and of negligible toxicity. The study has demonstrated that Fe_3BO_6 possesses low potential of redox reaction vs. Li/Li^+, which make it suitable for anode material for lithium-ion battery. It is very interesting that the initial norbergite structure of Fe_3BO_6 does not allow topotactic intercalation of lithium, but a structure transformation occurs on first discharge [11,12]. The compound undergoes framework disintegration, yielding amorphous phase that can be cycled with high reversibility. In the report of Ibarra-Palos and co-workers [12], the Fe_3BO_6 has capacity retention of about 225 mAh g^{-1} after 10 cycles. However, the electrochemical properties of Fe_3BO_6 in previous work were all tested at rather low current densities (10 and 5 mA g^{-1}, respectively), which limits its potential applications.

Generally, particle size and morphology are important factors that affect the electrochemical performance of the materials [1,13]. The use of smaller particles in electrodes could not only reduce the diffusion length for lithium insertion but also decrease the charge-transfer resistance of the electrodes. Additionally, the smaller particles can effectively increase the exposed surface area to favor Li-ion mobility with the electrode. Less solid-electrolyte interface (SEI) film is formed during the first discharge of spherical particles since they have the smallest specific surface area, thus the initial coulombic efficiency can be increased. Therefore, in order to achieve enhanced capacity and improve the fast rate performance, the spherical materials in the nanometer scale offer a feasible means.

As the traditional process [11,14], the iron borate compounds are usually prepared by solid-state reaction, which requires time-consuming processes, calcination at high temperatures or repeated heat treatment. In a solid-state reaction process to synthesize Fe_3BO_6, the diffusion rate of ions is rather slow, and it is difficult to make a homogenous phase. Thus, there often need a long sintering time to get the final product at high temperature.

In this work, we introduced the rheological phase reaction method to synthesize Fe_3BO_6 as anode material for lithium-ion battery. The as-prepared samples are spherical nanocrystals. The rheological phase reaction method is a novel method, which is a simple, economical and efficient soft chemistry method to prepare various functional materials such as photoluminescent materials

* Corresponding author. Fax: +86 27 68754067.
E-mail address: ljyuan@whu.edu.cn (L. Yuan).

0022-4596/$ - see front matter © 2008 Elsevier Inc. All rights reserved.
doi:10.1016/j.jssc.2008.05.025

[15,16], electrode materials [17,18] and magnetic materials [19,20]. Rheological phase reaction method is a process for preparing compounds or materials from a solid–liquid rheological mixture. The solid reactants were fully mixed in a proper molar ratio firstly. Then a proper amount of liquid substance (such as water or ethanol, etc.) was added to form a solid–liquid rheological body in which the solid particles and liquid substance were uniformly distributed. After the treatment of reactants under suitable conditions, the final product is obtained. In the rheological phase reaction method, the surface area of the solid particles can be utilized efficiently, and the contact between solid particles and fluid is close and uniform. Therefore, heat exchange is very efficient, and local overheating can be avoided. In the current rheological phase reaction system, the dissolved H_3BO_3 diffuses into the interspace of solid particles, H_3BO_3 and $FeC_2O_4 \cdot 2H_2O$ are homogeneously mixed at atomic scale, which is beneficial to the diffusion process and reaction process.

In comparison to solid-state synthesis for Fe_3BO_6, the rheological phase reaction method does not contain troublesome processes such as quenching, regrinding and repeated sintering, and the calcination time is only 5 and 3 h at temperature of 800 and 900 °C, respectively, which is much shorter than that of solid-state reaction method (880 °C, 48 h). The electrochemical performances of spherical Fe_3BO_6 nanoparticles obtained at different temperatures were investigated in detail. The materials display good rate performance at a relatively higher current density.

2. Experimental section

Fe_3BO_6 anode material was synthesized by the rheological phase reaction method. $FeC_2O_4 \cdot 2H_2O$ and H_3BO_3 were used as starting materials and were mixed by grinding in a molar ratio of 3:1.2 (0.2 molar of boron being in excess). A proper amount of deionized water was added to obtain a rheological body. The mixture was transferred into a Teflon container and the container was then sealed in a stainless autoclave at 80 °C for 5 h. After being dried at 80 °C, the precursor was moved into a quartz tube and sintered at different temperatures in flowing oxygen (0.1 L min^{-1}), and then cooled to room temperature naturally. The oxygen flow was used to favor the Fe^{3+} oxidation state in the reaction medium. The obtained products were washed with hot distilled water to remove the possible unreacted boron oxide.

The X-ray diffraction (XRD) patterns were obtained by Shimadzu XRD-6000 diffractometer with a Ni filter and Cu $K\alpha 1$ radiation ($\lambda = 1.54056$ Å). The thermogravimetry (TG) and differential thermal analysis (DTA) were carried out on PerkinElmer Thermal Analysis simultaneous thermal analyzer from room temperature to 1200 °C at a heating rate of 5 °C min^{-1} in a flow of air. X-ray photoelectron spectroscopy (XPS) measurements were performed on a KRATOS XSAM800 photoelectron spectrometer with an exciting source of Mg $K\alpha$ ($Ex = 1253.6$ eV). The morphologies and sizes of the products were investigated by scanning electron microscopy (SEM; FEI QUANTA 200 30 kV).

Electrochemical tests were carried out in a coin-type cell (size: 2016), which consisted of a Fe_3BO_6 working electrode and a lithium foil counter electrode separated by a Celgard 2400 microporous membrane. The working electrodes were prepared by a slurry procedure. The slurry consisted of 70 wt% active materials, 20 wt% acetylene black and 10 wt% polytetrafluoroethylene (PTFE) binder. $LiPF_6$ solution of 1 M in a 1:1 (v/v) mixture of ethylene carbonate (EC) and dimethyl carbonate (DMC) was used as electrolyte. The cells were assembled in an argon-filled glove box (Mikrouna-China Super 1220/750). The electrochemical properties were examined using Neware cell test system at 25 °C. Ac impedance measurements were performed using CHI660A by applying an ac voltage of 5 mV amplitude in the frequency range from 1 to 10 MHz.

3. Results and discussion

Thermal behaviors of the precursor after rheological phase reaction treatment are presented in Fig. 1. The precursor suffers a weight loss of 8.56% before 154 °C, which is due that the H_3BO_3 loses one molecular water to give HBO_2, with a corresponding endothermic peak observed near 132 °C. Between the temperature of 155 and 186 °C, HBO_2 releases water to produce $H_2B_4O_7$. There is a corresponding endothermic behavior near 165 °C. The third mass loss occurs in the region of 187–260 °C, which is ascribed to the loss of two molecular water of crystallization in $FeC_2O_4 \cdot 2H_2O$, with a corresponding endothermic peak observed near 228 °C. The pronounced weight loss process occurring at temperature between 275 and 502 °C is complicated. The exothermic peak at about 331 °C may be composed of three different thermal behaviors: $H_2B_4O_7$ decomposes to B_2O_3 and water, and FeC_2O_4 to $FeCO_3$ and CO; and then $FeCO_3$ further decomposes into FeO and CO_2. Although the decomposition of $H_2B_4O_7$ is an endothermic process, the simultaneous decomposition of FeC_2O_4 releases a lot of heat, thus leading to a strong exothermic peak on the DTA curve. The observed weight loss (30.28%) is consistent with the calculated value (31.93%). Along with heating, FeO is oxided to Fe_2O_3; B_2O_3 begins to melt, and react with Fe_2O_3 to produce Fe_3BO_6. This process is corresponding to the endothermic behavior around 612 °C, at which the crystallization of Fe_3BO_6 starts. This process can be seen clearly from the enlargement of the TG–DTA curves (inset in Fig. 1). During this process, there is a weight loss of about 2.20% due to the volatilization of a little amount of melting B_2O_3. Between the temperature of 750 and 900 °C, there is no weigh loss on the TG curve and no thermal peak on DTA, it can be concluded that the formed Fe_3BO_6 is stable in this range of temperature. When the temperature is enhanced, an endothermic peak emerges at around 1094 °C. This is because that Fe_3BO_6 begins to decompose at around 950 °C and gives birth to Fe_2O_3 and B_2O_3. This result is in agreement with that of Ibarra-Palos et al. [12]. Meanwhile, a slow weight loss observed on TG curve is because of the volatilization of B_2O_3.

The XRD pattern of precursor after rheological phase reaction treatment is shown in Fig. 2(a), which indicates that the precursor after rheological phase reaction treatment is still composed of

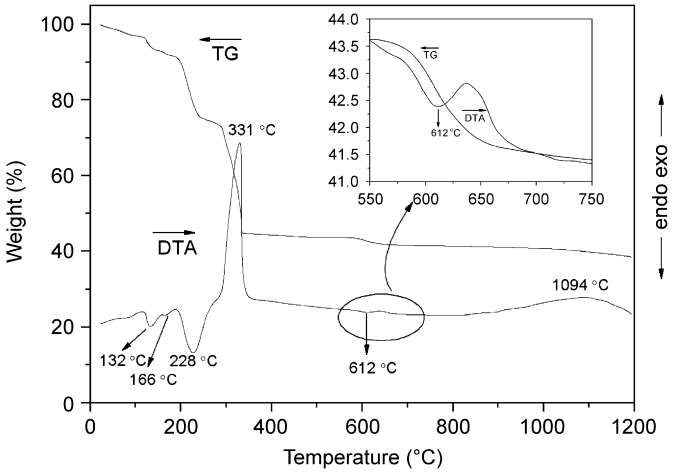

Fig. 1. TG and DTA curves of precursor after rheological phase reaction treatment in flowing air. Inset shows the enlargement of the TG–DTA curves between the temperature of 550 and 750 °C.

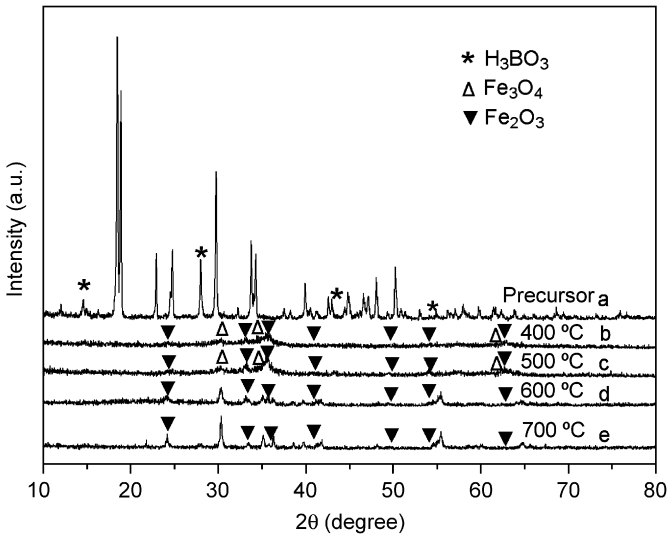

Fig. 2. XRD patterns of (a) precursor after rheological phase reaction treatment, and precursor after rheological phase reaction treatment sintered at (b) 400 °C, (c) 500 °C, (d) 600 °C, and (e) 700 °C.

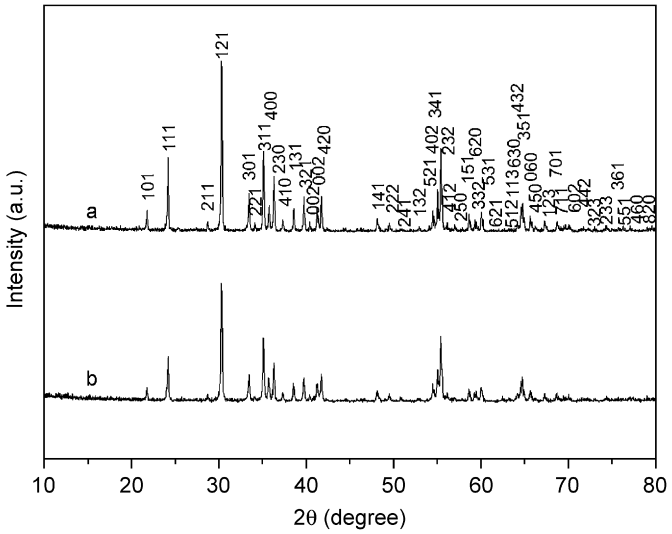

Fig. 3. The XRD patterns of Fe_3BO_6 powders obtained at different temperatures: (a) S-900 and (b) S-800.

H_3BO_3 and $FeC_2O_4 \cdot 2H_2O$. Asterisks indicate the main diffraction peak of H_3BO_3 in precursors. XRD patterns of the precursor sintered at different temperatures such as 400, 500, 600 and 700 °C are illustrated in Fig. 2. No diffraction peaks of B_2O_3 are detected at 400 °C and the temperature above, which indicates that B_2O_3 exists in an amorphous phase. The diffraction peaks of Fe_3O_4 and Fe_2O_3 can be found in the samples obtained at temperatures of 400 and 500 °C. When temperature is enhanced to 600 °C, the diffraction peaks of Fe_3BO_6 appear. Fe_3BO_6 coexists with Fe_2O_3 in the samples heated at 600 and 700 °C.

XRD patterns of the powders sintered at 800 °C for 5 h and 900 °C for 5 h (noted as S-800 and S-900) are shown in Fig. 3, respectively. Phase-pure Fe_3BO_6 is formed after calcination at 800 °C. No impurity phases are detected in the patterns of S-800 and S-900. All diffraction lines of samples can be indexed as the orthorhombic structure with *Pnma* space group. With the enhancement of calcination temperature, the intensity of diffraction peaks of samples is increased. The refined lattice parameters of S-800 and S-900 are $a = 10.036(4)$ Å, $b = 8.524(6)$ Å, $c = 4.460(5)$ Å, $V = 381.63$ Å^3 and $a = 10.034(5)$ Å, $b = 8.525(4)$ Å, $c = 4.460(7)$ Å, $V = 381.62$ Å^3, respectively, which are in good agreement with literature data (JCPDS no. 70-880).

Based on the thermal analysis of precursor and XRD patterns obtained at different temperatures above, we proposed the reaction process listed as follows:

(1) *The dehydration of H_3BO_3 and decomposition of $FeC_2O_4 \cdot 2H_2O$*: FeO obtained from decomposition of $FeC_2O_4 \cdot 2H_2O$ is then oxidized to Fe_3O_4 and finally to Fe_2O_3.

$$2H_3BO_3 \rightarrow B_2O_3 + 3H_2O\uparrow$$

$$FeC_2O_4 \cdot 2H_2O \rightarrow FeO + CO\uparrow + CO_2\uparrow + 2H_2O\uparrow$$

$$6FeO + O_2 \rightarrow 2Fe_3O_4$$

$$4Fe_3O_4 + O_2 \rightarrow 6Fe_2O_3.$$

(2) *Reaction of B_2O_3 and Fe_2O_3*: B_2O_3 melts at high temperature, and coats on the surface of Fe_2O_3 granules, and then the melting B_2O_3 reacts with Fe_2O_3 rapidly to form Fe_3BO_6.

$$3Fe_2O_3 + B_2O_3 \rightarrow 2Fe_3BO_6$$

The XPS spectra of Fe_3BO_6 nanospheres are shown in the Figs. 4(a)–(c). Maximum are observed at 711.2 and 724.8 eV in Fig. 4(a), which attributed to the binding energy of 2*p*3/2 and 2*p*1/2 for Fe (3+), respectively. No other valences of Fe appeared in the XPS spectra, which provides evidence that the Fe (2+) in precursor is fully oxidized to Fe (3+) by heat treatment in the flow of oxygen. In Figs. 4(b) and (c), the peaks located at 191.7 and 530.8 eV are assigned to B 1*s* and O 1*s*, respectively.

Fig. 5 provides the typical SEM images of the obtained Fe_3BO_6 powders. The sizes and morphologies of the S-800 and S-900 are different, respectively. The sample of S-800 consists of well-spherical particles with a uniform size about 40 nm. These particles stand freely in a monodisperse state [see Fig. 5(a)]. Fig. 5(b) gives the SEM photographs of the sample of S-900. The powders are smooth and uniform nanospherical particles with a diameter of 100–500 nm. The grains agglomerate randomly. It is obvious that the particle size increases with increasing of the calcination temperature.

As mentioned above, the particle size determines the effective surface area and smaller particles tend to improve the capacity of a battery by reducing the ion diffusion pathway during intercalation–deintercalation process. On the other hand, the uniform particle size distribution leads to the uniform depth of discharge (DOD) of each particle, which increases the utilization of the material to enhance the overall battery performance. The particle features of S-800 are favorable for the intercalation–deintercalation reaction of electrode on the anode surface during the discharge–charge process, and this sample is expected to deliver a higher capacity. Whereas, the increased exposed surface area may increase the unpredictable reaction between the electrode and electrolyte, and may lead to safety problems, for example, poor overcharge performance.

The initial discharge–charge profiles of obtained Fe_3BO_6 nanospheres are presented in Fig. 6. There are wide plateaus on the first discharging curves. The plateaus on the discharging curves correspond to the structural changes in the discharging process [11]. The norbergite structure of Fe_3BO_6 [11] decomposes into an amorphous material on first discharge, which is a unique characteristic of Fe_3BO_6 compound. S-800 shows a higher plateau potential at 1.41 V than S-900 (1.27 V). The working voltage for the

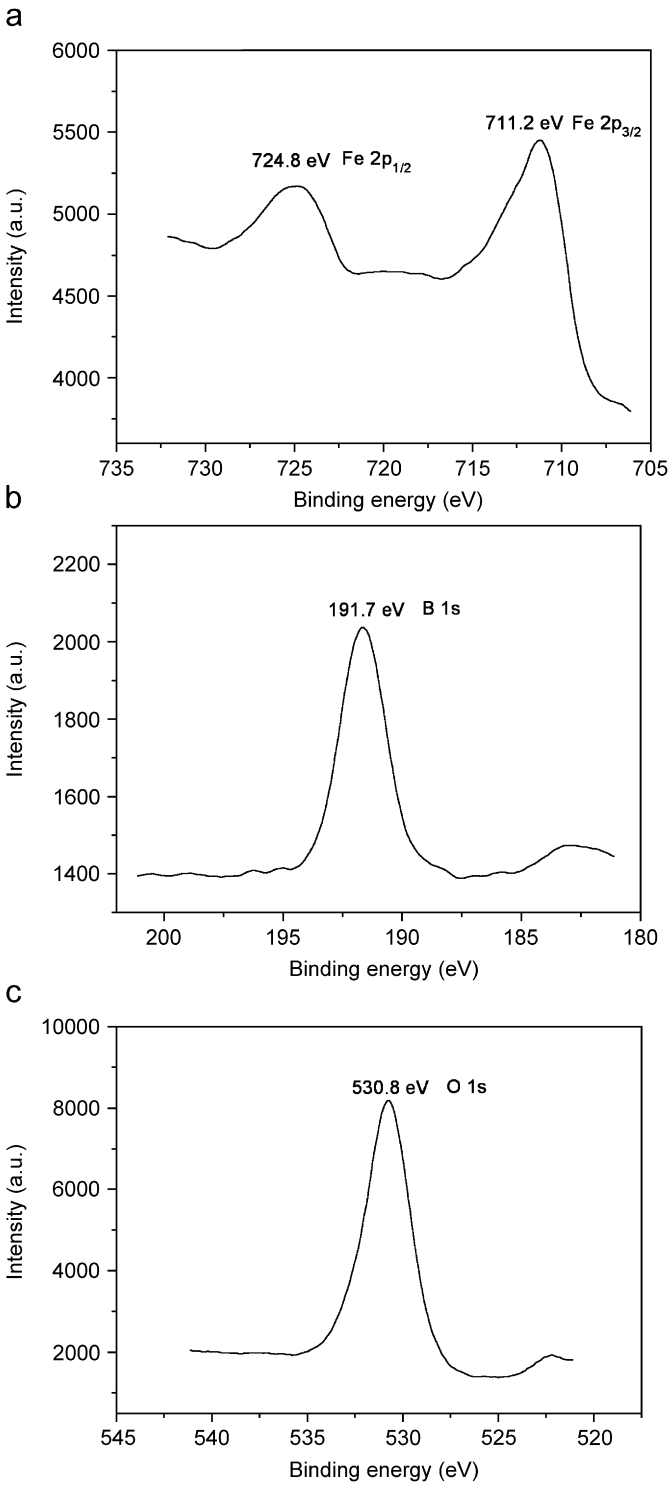

Fig. 4. XPS spectra for Fe_3BO_6 nanospheres: (a) Fe 2*p*, (b) B 1*s* and (c) O 1*s*.

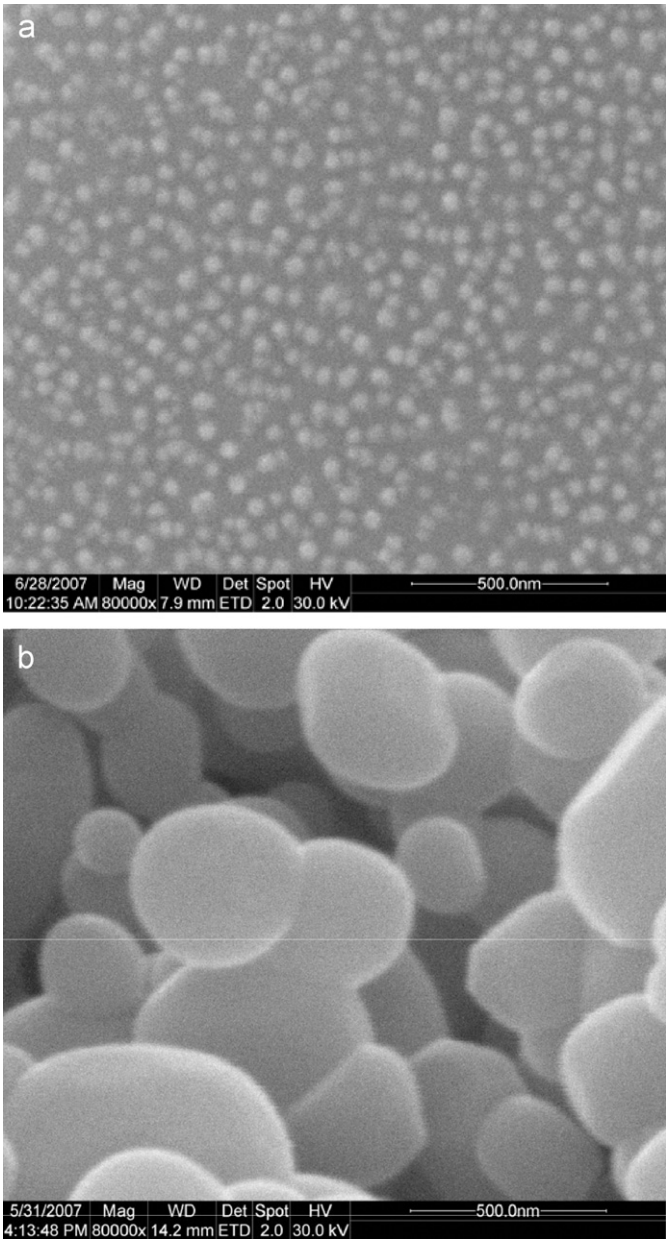

Fig. 5. SEM images of the Fe_3BO_6 powders: (a) S-800 and (b) S-900.

first discharge is higher than that of graphite (0.1 V) [21], and some alloys, such as $SnSbCu_x$ (around 0.7 V) [22], SnSb (0.8 V) [23]. As for S-900, it shows a plateau potential at 1.40 V when the current density decreases to 10 mA g^{-1}, which is shown in Fig. 6(c). The data demonstrated that the plateau potential on the initial discharge was enhanced when the active material had a reduced particle size or the current density became lower. The reason may be attributed to the decrease of electrode polarization. When the voltage window was broadened to 0.6 and 3.1 V at a current density of 100 mA g^{-1}, the plateau was changed to 1.30 V [Fig. 6(d)]. The discharge–charge profiles of Fe_3BO_6 electrodes (S-900) are illustrated in Fig. 7. It can be seen that the working voltage for the first discharge is around 1.3 V, the following discharges occur at the higher potential (about 1.5 V), and their curves have slopes in the latter case.

Table 1 lists the electrochemical performance of the Fe_3BO_6 electrodes. In the table, coulombic efficiency is the ratio of initial charge capacity relative to the initial discharge capacity. $R_{10/1}$ is the ratio of charge capacity in the 10th cycle relative to the 1st, which indicates the material cycleability [24]. Fig. 8 presents the cycling performance of Fe_3BO_6 electrodes. S-800 delivers the initial discharge and charge capacity of 874 and 557 mAh g^{-1} with a coulombic efficiency of 64%. S-800 delivers a high reversible capacity and still remains above 500 mAh g^{-1} after several cycles, which is higher than that of Fe_3BO_6 prepared by a traditional solid-state reaction [11,12]. S-900 delivers the lower initial discharge and charge capacity but higher coulombic efficiency

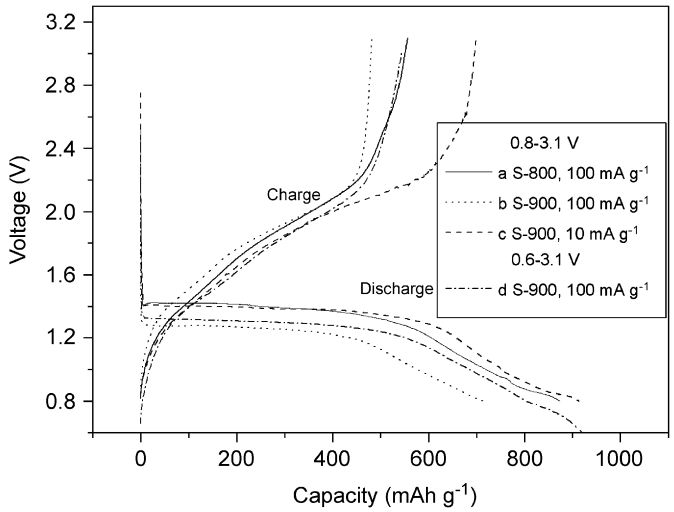

Fig. 6. First cycle profiles of Fe_3BO_6 electrodes under different electrochemical test conditions: (a) S-800, 100 mA g^{-1}, (b) S-900, 100 mA g^{-1}, (c) S-900, 10 mA g^{-1} cycled between 0.8 and 3.1 V, and (d) S-900, 100 mA g^{-1}, cycled between 0.6 and 3.1 V.

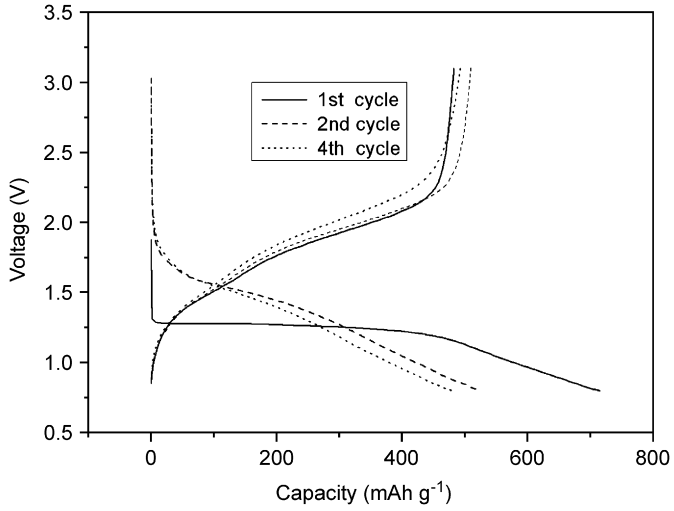

Fig. 7. Cycle profiles of Fe_3BO_6 electrodes (S-900) cycled at 100 mA g^{-1}, between 0.8 and 3.1 V.

Table 1
Electrochemical performances of Fe_3BO_6 under different electrochemical test conditions: (a) S-800, 100 mA g^{-1}, (b) S-900, 100 mA g^{-1}, (c) S-900, 10 mA g^{-1} cycled between 0.8 and 3.1 V and (d) S-900, 100 mA g^{-1}, cycled between 0.6 and 3.1 V

	a	*b*	*c*	*d*
1st discharge capacity (mAh g^{-1})	874	715	914	921
1st charge capacity (mAh g^{-1})	557	482	700	544
Coulombic efficiency (%)	64	67	77	59
$R_{10/1}$ (%)	75	78	59	58

than S-800. The charge capacity of the S-900 gradually reduces with the cycle number. The capacity retention ($R_{10/1}$) of S-900 is 78%, which is higher than that of S-800 (75%). As for S-800, the smaller particle size than S-900 means a larger active area to the reaction between electrolyte and anode material, thus lead to the lower $R_{10/1}$ value than S-900.

Compared with the published results, the reversible capacity and cycleability of Fe_3BO_6 obtained by the rheological phase reaction method are improved. The capacity reported by Strobel et al. [12] is only about 225 mAh g^{-1} after 10 cycles. Moreover,

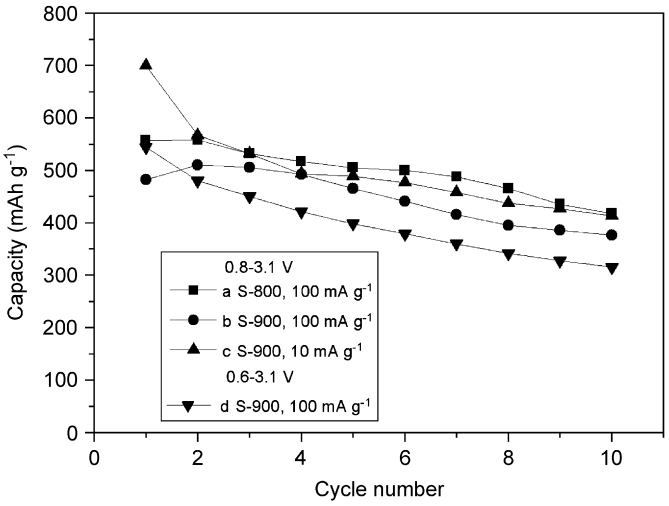

Fig. 8. Cycling performance of Fe_3BO_6 under different electrochemical test conditions: (a) S-800, 100 mA g^{-1}, (b) S-900, 100 mA g^{-1} and (c) S-900, 10 mA g^{-1} cycled between 0.8 and 3.1 V and (d) S-900, 100 mA g^{-1}, cycled between 0.6 and 3.1 V.

S-800 delivers higher reversible capacity (>500 mAh g^{-1}) than those of published by Nazar et al. [11] (<450 mAh g^{-1}) in the first several cycles.

We investigated the influence of different electrochemical test conditions on S-900. Compared of electrochemical performances tested at the different current density of 100 and 10 mA g^{-1}, it is believed that the low current density favors the higher initial discharge/charge capacity and coulombic efficiency. In addition, the reversible capacity is higher but the $R_{10/1}$ value is lower at the current density of 10 mA g^{-1}. S-900 cycled between 0.8 and 3.1 V has an initial discharge and charge capacities of 715 and 482 mAh g^{-1}, respectively, with a coulombic efficiency of 67%. When the voltage cut-off was reduced from 0.8 to 0.6 V, the initial discharge and charge capacities increased to 921 and 544 mAh g^{-1}, respectively, with a coulombic efficiency of 59%. This illustrated that the DOD results in the increase of the initial discharge and charge capacities but brings about the decrease of coulombic efficiency.

The electrochemical impedance spectra (EIS) of S-800 and S-900 were measured. Fig. 9(a) shows the EIS of S-800 and S-900 electrodes at the discharged state (0.8 V) in the first cycle. In general, R_s is the electrolyte resistance of the cell. R_{sei} is the resistance of SEI layer formed on the surface of the electrodes, which corresponds to the semicircle at high frequencies. The semicircle in medium-frequency region is attributed to the charge-transfer resistance (R_{ct}) on electrode/electrolyte surface. And the straight sloping line at the low-frequency end is assigned to the lithium-diffusion process at the interface between the active material particles and electrolyte. Both spectra have two semicircles in the high- and medium-frequency region, but they are distinctly different. It is clear that the S-800 has higher R_{sei} value and much lower R_{ct} value than S-900. It is speculated that with the decrease of particle size, the surface area is increased and the R_{sei} value is then become higher. For a noticeable decrease in the R_{ct} of S-800 than S-900, it is because smaller grain size with a monodisperse morphology in S-800 can favor Li^+ ions mobility in the particles by shortening the ion diffusion pathway, S-800 becomes more conductive than S-900. In order to investigate the reason for the capacity fade on cycling, the impedance spectra of S-900 measured at 0.8 V after the first and tenth cycle discharge are illustrated in Fig. 9(b). After 10 cycles, the impedance of surface film shows little change while the impedance of charge-

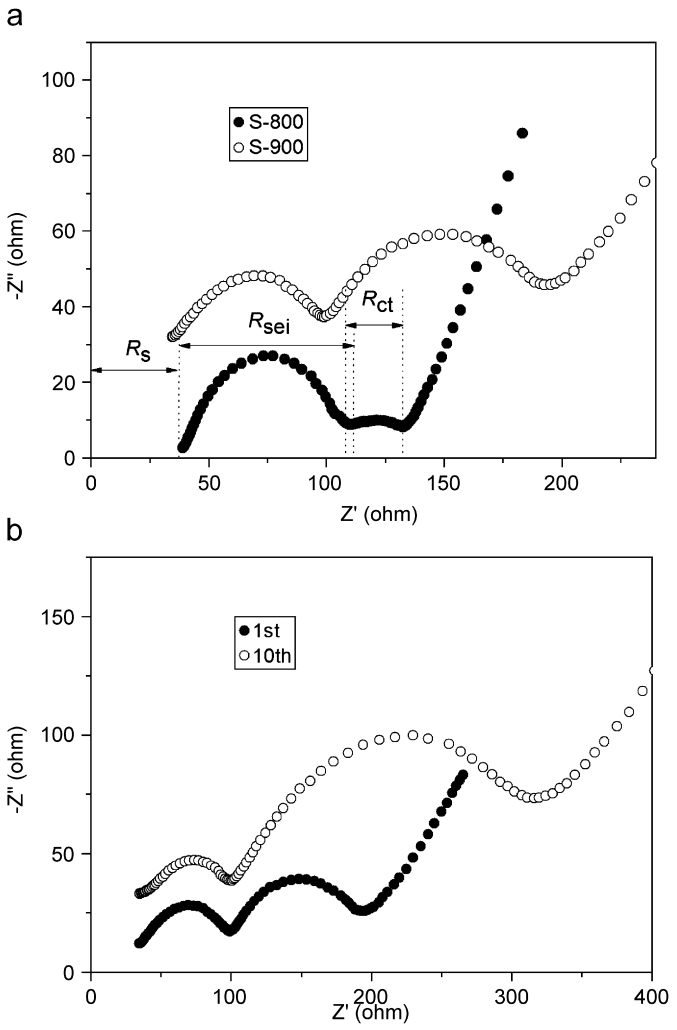

Fig. 9. The ac impedance spectra of Fe_3BO_6 electrodes at room temperature: (a) S-800 and S-900 at 0.8 V after first discharge and (b) S-900 at 0.8 V after the first and tenth discharge, respectively. Frequency range from 1 MHz to 10 mHz.

transfer reaction increases a lot. Therefore, it can be presumed that the increase of R_{ct} results in the capacity fading during cycling.

4. Conclusion

In summary, we have developed the rheological phase reaction method, which is simple and rapid to synthesize the spherical Fe_3BO_6 nanoparticles. Different size and morphology can be obtained by varying calcination temperature. The spherical Fe_3BO_6 nanoparticles synthesized at different temperatures were found to have different electrochemical performances. S-800 delivers a high reversible capacity of above 500 mAh g^{-1}. S-900 gives the lower reversible capacity than S-800, but possesses a relatively good cycle life. Smaller Fe_3BO_6 nanoparticles intend to give higher R_{sei} value and much lower R_{ct} value after the first discharge by the measurement of EIS. In addition, it is presumed that the increase of R_{ct} is the possible reason for the capacity fading during cycling.

Acknowledgment

Support of this work by the National Natural Science Foundation of China is gratefully acknowledged (no. 20671074).

References

[1] K. Zaghib, X. Song, A. Guerfi, R. Kostecki, K. Kinoshita, J. Power Sources 124 (2003) 505–512.
[2] Y. Yu, C.H. Chen, Y. Shi, Adv. Mater. 19 (2007) 993–997.
[3] M.C. Tucker, M.M. Doeff, T.J. Richardson, R. Finones, E.J. Cairns, J.A. Reimer, J. Am. Chem. Soc. 124 (2002) 3832–3833.
[4] F. Sauvage, E. Baudrin, L. Laffont, J.M. Tarascon, Solid State Ionics 178 (2007) 145–152.
[5] S. Komaba, K. Suzuki, N. Kumagai, Electrochemistry 70 (2002) 506–510.
[6] D. Larcher, D. Bonnin, R. Cortes, I. Rivals, L. Personnaz, J.M. Tarascon, J. Electrochem. Soc. 150 (2003) A1643–A1650.
[7] M. Manickam, P. Singh, T.B. Issa, S. Thurgate, K. Prince, Electroceram. Jpn ix key Eng. Mater. 320 (2006) 271–274.
[8] S. Ito, K. Nakaoka, A. Kawamura, K. Ui, K. Fujimoto, N. Koura, J. Power Sources 146 (2005) 319–322.
[9] Y.T. Lee, C.S. Yoon, Y.S. Lee, Y.-K. Sun, J. Power Sources 134 (2004) 88–94.
[10] P. Larsson, R. Ahuja, A. Nytén, J.O. Thomas, Electrochem. Commun. 8 (2006) 797–800.
[11] J.L.C. Rowsell, J. Gaubicher, L.F. Nazar, J. Power Sources 97–98 (2001) 254–257.
[12] A. Ibarra-Palos, C. Darie, O. Proux, J.L. Hazemann, L. Aldon, J.C. Jumas, M. Morcrette, P. Strobel, Chem. Mater. 14 (2002) 1166–1173.
[13] F. Zhou, X.M. Ni, Y.F. Zhang, H.G. Zheng, J. Colloid Interface Sci. 307 (2007) 135–138.
[14] J.C. Joubert, T. Shirk, W.B. White, R. Roy, Mater. Res. Bull. 3 (1968) 671–676.
[15] M.C. Yin, L.J. Yuan, C.C. Ai, C.W. Wang, Polyhedron 23 (2004) 529–536.
[16] M.C. Yin, J.T. Sun, J. Alloys Compd. 381 (2004) 50–57.
[17] C.W. Wang, X.L. Ma, Z.C. Li, Y.G. Liang, J.T. Sun, Y.H. Zhou, Electrochem. Commun. 8 (2006) 289–292.
[18] C.W. Wang, X.L. Ma, L.Q. Zhou, J.G. Cheng, J.T. Sun, Y.H. Zhou, Electrochim. Acta 52 (2007) 3022–3027.
[19] C.J. Cong, L. Liao, Q.Y. Liu, J.C. Li, K.L. Zhang, Nanotechnology 17 (5) (2006) 1520–1526.
[20] C.J. Cong, L. Liao, J.C. Li, L.X. Fan, K.L. Zhang, Nanotechnology 16 (6) (2005) 981–984.
[21] T. Ohzukua, R.J. Brodd, J. Power Sources 174 (2007) 449–456.
[22] F. Wang, M. Zhao, X. Song, J. Power Sources 175 (2008) 558–563.
[23] L. Simonin, U. Lafont, E.M. Kelder, J. Power Sources (2008).
[24] J.Y. Lee, R.F. Zhang, Z.L. Liu, J. Power Sources 90 (2000) 70–75.